*J.Natn.Sci.Foundation Sri Lanka 2024 52 (3):* 385 - 400
DOI: http://dx.doi.org/10.4038/jnsfsr.v52i3.11798

RESEARCH ARTICLE

## Environmental Chemistry

# Effective removal of Pb(II) ions using $Fe_3O_4$/MgO adsorbent: A comprehensive study

**V Gurunanthanan[1], KB Wijayaratne[2], BS Dassanayake[2], PG Mantilaka[1], and CS Perera[2*]**
[1] *Postgraduate Institute of Science, University of Peradeniya, Peradeniya, Sri Lanka.*
[2] *Department of Physics, Faculty of Science, University of Peradeniya, Peradeniya, Sri Lanka.*

Submitted: 04 August 2023; Revised: 23 March 2024; Accepted: 19 April 2024

**Abstract:** The effective removal of heavy metal ions, particularly Pb(II), from contaminated water sources remains a pressing environmental concern. This study explores the potential of $Fe_3O_4$/MgO nanocomposite as an efficient adsorbent for selective Pb(II) removal. The $Fe_3O_4$/MgO nanocomposite was synthesized using a controlled sol-gel method and characterized using various techniques. X-ray diffraction (XRD) analysis confirmed the presence of cubic MgO and cubic $Fe_3O_4$. Pb(II) adsorption induced a crystallographic transformation, forming hexagonal $Mg(OH)_2$ crystals, indicating interaction with the adsorbent. Scanning electron microscope (SEM) analysis revealed pyramid-like and irregular crystal morphologies. Pyramid-like structures provided a larger surface area and active sites for effective Pb(II) interaction, while irregular crystal particles, representing magnetic $Fe_3O_4$, contributed to stability and dispersibility. Vibrating sample magnetometer (VSM) results confirmed superparamagnetic behaviour with a saturation magnetization of 32.02 emu $g^{-1}$, indicating potential for magnetic separation and recovery in various wastewater treatment applications. Adsorption experiments utilized optimized conditions: an initial concentration of 600 $mgL^{-1}$, adsorbent dosage of 0.25 $gL^{-1}$, pH of 7, and 120 minutes of reaction time. The $Fe_3O_4$/MgO nanocomposite exhibited exceptional performance with a remarkable 99.98% removal efficiency and a high adsorption capacity of 2399.44 mg $g^{-1}$. These impressive results underscore the outstanding adsorption potential of the nanocomposite. Adsorption kinetics followed the pseudo-second-order model ($R^2$ = 0.99), confirming suitability for Pb(II) removal. The Freundlich model indicated a heterogeneous surface with different adsorption sites. Overall, the $Fe_3O_4$/MgO nanocomposite exhibits potential as a cost-effective, environmentally friendly adsorbent for removing Pb(II) ions, providing a promising solution for water purification and environmental remediation.

**Keywords:** Adsorption capacity, chemisorption, environmental remediation, heterogeneous surface, sol-gel method, superparamagnetic behaviour.

## INTRODUCTION

Lead (Pb) contamination in water sources poses a significant threat to human health and the environment due to its toxic nature and potential long-term effects. Exposure to Pb(II) ions can lead to various adverse health outcomes, particularly in children, including neurological damage, developmental disorders, and impaired cognitive functions (Lidsky & Schneider, 2003). Therefore, the development of efficient and sustainable methods for the removal of Pb(II) from contaminated water is of utmost importance. In recent years, nanomaterial-based adsorbents have shown great promise in the removal of heavy metals from aqueous solutions (Perera *et al*., 2024). Among these nanomaterials, $Fe_3O_4$/MgO nanocomposite has emerged as highly effective adsorbents for Pb(II) removal. The combination of $Fe_3O_4$ and MgO in a nanocomposite offers synergistic effects, leveraging the magnetic properties of $Fe_3O_4$ and the excellent adsorption capacities and chemical stability of MgO. $Fe_3O_4$/MgO nanocomposite provides a versatile platform for the

* Corresponding author (chanip@sci.pdn.ac.lk; https://orcid.org/0000-0001-8644-7396)

adsorption of Pb(II) ions through various mechanisms, including surface interactions, ion exchange, and complexation. The magnetic properties of $Fe_3O_4$ facilitate easy separation and recyclability of the nanocomposite, minimizing secondary pollution and enabling repeated use (Sameera *et al*., 2023). This makes $Fe_3O_4$/MgO nanocomposite highly suitable for practical applications in water treatment. Previous studies have demonstrated the effectiveness of $Fe_3O_4$/MgO nanocomposite in removing other heavy metals and dyes. For instance, Habiby *et al.* (2019) reported an adsorption capacity of 2.5 mg $g^{-1}$ and a removal efficiency of 98.9% for phosphate, using chemical precipitation by synthesized $Fe_3O_4$/MgO nanocomposite. Similarly, Namvar-Mahboub *et al.* (2020) achieved removal efficiency of 98.2% and 95.5% for Pb(II), and Cd(II) using green synthesized $Fe_3O_4$/MgO nanocomposite, respectively. These findings underscore the potential of $Fe_3O_4$/MgO nanocomposite as efficient adsorbent for heavy metal removal. In another study by Nagarajah *et al.* (2017), MgO cores with silica-coated nano $Fe_3O_4$ nanocomposite demonstrated exceptional performance in the removal of Pb(II) from aqueous solutions, compared with Cd(II) and Cu(II). The adsorption capacity of these nanocomposites for Pb(II) was found to be as high as 238 mg $g^{-1}$, highlighting their superior adsorption capability. These findings emphasize the significant potential of $Fe_3O_4$/MgO nanocomposite as efficient adsorbent for Pb(II) removal. However, there is a need for further investigation to explore the adsorption capacity, kinetics, and mechanisms of Pb(II) removal using $Fe_3O_4$/MgO nanocomposites. Understanding the influence of various parameters, such as pH, initial Pb(II) concentration, contact time, and temperature, on the adsorption process is crucial for optimizing the design of water treatment systems. We have modified the synthesis procedure based on the work conducted by Salem & Ahmed (2016), where they utilized this material for the removal of amaranth dye using adsorption studies. In our study, we have adapted this modified procedure to target the removal of Pb(II) ions, aiming to enhance the adsorption capacity compared to the existing literature. In this study, we aim to investigate the potential of $Fe_3O_4$/MgO nanocomposite as an efficient adsorbent for the removal of Pb(II) from aqueous solutions. The study evaluates the adsorption capacity, kinetics, and isotherms of Pb(II) adsorption onto $Fe_3O_4$/MgO nanocomposite. Additionally, the reported work will explore the effects of different experimental parameters on the adsorption process to optimize the removal efficiency. The insights gained from this research will contribute to the development of sustainable and effective strategies for Pb(II) removal from contaminated water sources.

## MATERIALS AND METHODS

### Materials

The chemicals used were iron (II) chloride tetrahydrate ($FeCl_2 \cdot 4H_2O$), iron (III) chloride hexahydrate ($FeCl_3 \cdot 6H_2O$, Loba Chemie), magnesium chloride hexahydrate ($MgCl_2 \cdot 6H_2O$, Hopkin and Williams LTD.), cetyltrimethylammonium bromide (CTAB, Research Lab Fine Chem Industries), ammonia ($NH_4 \cdot OH$, Loba Chemie), ethanol ($C_2H_5OH$, VWR chemicals), silver nitrate ($AgNO_3$, Loba Chemie), and lead nitrate ($Pb(NO_3)_2$, Hemas(Drugs) Ltd.). All the substances utilized were of analytical grade. Deionized distilled water was employed in the preparation of all solutions.

### Synthesis of $Fe_3O_4$/MgO nanocomposite

A modified synthesis procedure based on the work done by Salem & Ahmed (2016) was followed. $Fe_3O_4$/MgO nanocomposite was prepared using a controlled sol-gel method as described below. Initially, approximately 1 mL of cetyltrimethylammonium bromide (CTAB) solution, a cationic surfactant above its critical micelle concentration, was added to a 50 mL solution of 1 M $MgCl_2$ with constant stirring for 1 h. Subsequently, a 1 M ammonia solution was added drop by drop to the $MgCl_2$ solution until the clear solution turned into a white sol of $Mg(OH)_2$. The sol was stirred for an additional 2 h and left undisturbed for two days to allow for the condensation of sol particles into solid gel nanoparticles. The gel particles were collected through filtration and thoroughly washed with distilled water multiple times to remove chloride ions. The effectiveness of the washing process was confirmed when the filtrate yielded a negative test result with silver nitrate solution. After washing, the final product was dried at 90 °C overnight. The dried powders were then subjected to calcination in a high-temperature furnace at 400 °C for 2 h to induce the crystallization of MgO nanoparticles. In parallel, $Fe_3O_4$ nanoparticles were prepared by mixing an appropriate amount of ferrous chloride and ferric chloride solutions. Iron(II) chloride ($FeCl_2$, 1.9 g) and iron(III) chloride ($FeCl_3$, 3.2 g) were dissolved in 50 mL of deionized water at a molar ratio of 1:2 to prepare the $Fe_3O_4$ precursor solution. The solution was stirred using a magnetic stirrer until the iron salts were completely dissolved. Ammonia solution was added to the mixture until a black precipitate was detected, indicating the formation of $Fe_3O_4$. The magnetite solution was subsequently separated using magnetic separation and washed with distilled water. The $Fe_3O_4$

nanoparticles were then dried at 105 °C for 24 h. The synthesized $Fe_3O_4$ nanoparticles and MgO nanoparticles were combined. The $Fe_3O_4$/MgO nanocomposite was prepared with 46.29 wt % $Fe_2O_3$ 53.71 wt % Mgo and suspended in 50 mL of distilled water. Ultrasonication for 40 min was employed to promote the interaction between the two nanoparticle components, ensuring uniform dispersion and intimate contact. The $Fe_3O_4$/MgO nanocomposite was then separated from the suspension using magnetic separation and washed with deionized water to eliminate any residual impurities. Subsequently, the nanocomposites were dried at 90 °C for 24 h under controlled conditions to remove any remaining solvent and ensure their stability.

**Characterization of $Fe_3O_4$/MgO nanocomposite**

Various characterization techniques were employed to test the $Fe_3O_4$/MgO nanocomposite and analyze the Pb(II) adsorbed $Fe_3O_4$/MgO nanocomposite. X-ray Diffraction (XRD, D8 ADVANCE ECO - Bruker, CuKα λ = 0.154 nm, 2θ range of 20–80˚, step size of 0.02˚ and a step time of 1 s) analysis was used to identify the crystal structure and phase composition of the nanocomposite. scanning electron microscopy (SEM, Oxford/X-act, ZEISS, operated at 20 keV) was employed for the examination of the surface morphology and particle size distribution of the nanocomposite. Energy-dispersive X-ray spectroscopy (EDS, Oxford/X-act, ZEISS, operated at 20 keV) was used to determine the elemental composition of the nanocomposite. Fourier transform infrared spectroscopy (FTIR, Bruker VERTEX 80) analysis was used to identify the functional groups present in the nanocomposite while vibrating sample magnetometry (VSM, DXWD-60, and Xiamen Dexing Magnet Tech.Co.Ltd) was employed to investigate the magnetic properties of the nanocomposite. Atomic absorption spectroscopy (AAS, Shimadzu AA-7800) enabled the quantitative analysis of the concentration of Pb(II) ions in the solution before and after adsorption.

**Batch adsorption experiment**

Initially, $Fe_3O_4$/MgO nanocomposite was synthesized using a controlled sol-gel method, as described previously. The nanocomposite was then washed with deionized water and dried to ensure their stability. The optimization of adsorbent dosage was carried out by adding different amounts of the nanocomposite (ranging from 0.05 g $L^{-1}$ to 0.4 g $L^{-1}$) into separate solutions of 600 mg $L^{-1}$ concentration of Pb(II). The mixtures were agitated until adsorption equilibrium was reached, and the residual Pb(II) concentration was measured. Similarly, the optimization of initial concentration involved preparing different concentrations of Pb(II) solutions (ranging from 400 to 1000 mg $L^{-1}$) and adding 0.25 g $L^{-1}$ of the nanocomposite to each solution. The solutions were mixed to reach adsorption equilibrium, and the final Pb(II) concentrations were measured. The optimization of pH was accomplished by adjusting solutions of 600 mg $L^{-1}$ Pb(II) concentration to different pH levels (ranging from pH 4 to 10) using appropriate buffers. The 0.25 g $L^{-1}$ of nanocomposites were added, and the mixtures were agitated before measuring the final Pb(II) concentrations. The optimization of reaction time involved adding 0.25 g $L^{-1}$ of the nanocomposite to a solution of 600 mg $L^{-1}$ Pb(II) concentration and agitating the mixture for various time intervals ranging from 10 to 150 min. The residual Pb(II) concentrations were measured at each time interval.

To determine the equilibrium adsorption capacity and removal efficiency of Pb(II) ions using $Fe_3O_4$/MgO nanocomposite, batch adsorption experiments were conducted. An optimized mass of the nanocomposite was added to a Pb(II) ion solution of optimized initial concentration ($C_0$) and volume (V). The mixture was stirred continuously, and samples were taken at 10 min time intervals to measure the concentration of Pb(II) ions ($C_t$) using atomic absorption spectroscopy. The adsorption capacity ($q_t$) at each time interval was calculated using the formula $q_t = ((C_0 - C_t) \times V)/m$, where m is the mass of the adsorbent. The removal efficiency was calculated as removal efficiency (%) = $((C_0 - C_t) \times 100)/C_0$. The experiments continued until the system reached equilibrium, indicated by no significant change in $C_t$. In addition, various adsorption isotherm models, including Langmuir, Freundlich, and Temkin, were applied to the equilibrium data, while different kinetic models such as pseudo-first-order, pseudo-second-order, liquid film diffusion, and intraparticle diffusion were employed to analyze the kinetic data. Finally, the results obtained from the batch adsorption studies were analyzed to determine the optimum adsorbent dosage, initial concentration, pH, reaction time, and the adsorption isotherm and kinetic parameters associated with the removal of Pb(II) using $Fe_3O_4$/MgO nanocomposite.

## RESULTS AND DISCUSSION

**Scanning electron microscopy (SEM)**

The morphology and microstructure of the $Fe_3O_4$/MgO nanocomposite were thoroughly investigated using SEM (Supplementary Figure S1a). The SEM images of the $Fe_3O_4$/MgO nanocomposite revealed distinct

morphological features. The $Fe_3O_4$ nanoparticles exhibited an irregular crystal shape with varying sizes. Meanwhile, the pyramid-shaped MgO particles showed a unique morphology with sharp edges.

The combination of these two different morphologies created a highly interconnected and porous structure, potentially enhancing the material's adsorption capacity. The irregular crystal shape of $Fe_3O_4$ nanoparticles contributed to a higher surface area and provided numerous active sites for Pb(II) adsorption. Additionally, the presence of pyramid-shaped MgO particles improved the overall structural stability of the nanocomposite, making it suitable for long-term usage in environmental applications. The SEM images of the $Fe_3O_4$/MgO nanocomposite after Pb(II) adsorption revealed notable agglomeration of Pb(II) ions on the surfaces of both the irregular crystal-shaped $Fe_3O_4$ nanoparticles and the pyramid-shaped MgO particles (Supplementary Figure S1b). The irregular crystal-shaped $Fe_3O_4$ nanoparticles exhibited a greater propensity for Pb(II) adsorption due to their increased surface area and numerous active sites. As a result, the surfaces of these nanoparticles displayed significant clusters of Pb(II) ions. Similarly, the pyramid-shaped MgO particles also demonstrated agglomeration of Pb(II) ions, suggesting their involvement in the adsorption process. The unique morphology of the pyramid-shaped particles, with their sharp edges and interconnected structure, facilitated the accumulation of Pb(II) ions on their surfaces. The agglomeration phenomenon observed on the irregular crystal and pyramid-shaped surfaces indicates the strong affinity of the $Fe_3O_4$/MgO nanocomposite for Pb(II) ions. The adsorption capacity of the nanocomposite was likely enhanced by the combined effect of the irregular crystal-shaped $Fe_3O_4$ nanoparticles and the pyramid-shaped MgO particles, which provided ample binding sites and increased contact area for Pb(II) adsorption. These images provide visual evidence of the effective removal and accumulation of Pb(II) ions by $Fe_3O_4$/MgO nanocomposites. Moreover, the EDS analysis of the nanocomposite revealed the presence of Fe, O, and Mg elements with weight percentages of 28.97%, 25.55%, and 30.0%, respectively (Supplementary Figure S1c). This confirms the successful incorporation of these elements in the nanocomposite, supporting their potential in the efficient removal of Pb(II) ions from the water. EDS analysis performed after the adsorption of Pb(II) ions on the surface of $Fe_3O_4$/MgO nanocomposite confirmed the presence of Pb peaks, indicating successful binding of Pb(II) onto the adsorbent (Supplementary Figure S1d). The quantitative EDS data shown in Supplementary Table S1 reveals the incorporation of Pb(II) on the $Fe_3O_4$/MgO surface, further supporting the efficient removal of Pb(II) ions.

**X-ray diffraction (XRD)**

The XRD analysis of the synthesized $Fe_3O_4$/MgO nanocomposite is presented in Supplementary Figure S2a. The observed peaks at 2θ = 30.22°, 35.6°, 53.98°, and 57.23° indicate the presence of cubic $Fe_3O_4$ with (220), (311), (422), and (511) planes, respectively (JCPDS 01-084-2782). Furthermore, the peaks at 2θ = 37.06°, 43.06°, and 62.53° suggest the presence of cubic MgO (periclase) with (111), (200), and (220) planes, respectively (JCPDS 01-075-1525). Additionally, peaks at 2θ = 33.33°, and 49.69° indicate the presence of rhombohedral $Fe_2O_3$ with (104), and (024) planes, respectively (JCPDS 01-072-6225). Hence, our analysis confirms that the synthesized final product consists of cubic structures of $Fe_3O_4$ and periclase MgO. After adsorbing Pb(II) (Supplementary Figure S2b), a significant number of diffraction peaks were indexed to $Pb_3(CO_3)_2(OH)_2$. Peaks observed at 2θ = 24.67°, 41.28°, 49.8°, and 56.99° could be indexed to the presence of rhombohedral $Pb_3(CO_3)_2(OH)_2$ with (104), (211), (220), and (125) planes, respectively (JCPDS 01-073-4362). The peak observed at 2θ = 54.29° indicates the presence of tetragonal PbO with a (211) plane (JCPDS 01-085-1292). Peaks observed at 2θ = 33.45°, 35.8°, and 64.49° indicate the presence of rhombohedral $Fe_2O_3$ with (104), (110), and (300) planes, respectively (JCPDS 01-084-0311).

Peaks observed at 2θ = 38.28°, 58.97°, and 62.41° could be indexed to the presence of hexagonal $Mg(OH)_2$ with (011), (110), and (111) planes, respectively (JCPDS 01-086-0441). Peaks observed at 2θ = 30.38°, 37.43°, and 43.49° indicate the presence of cubic $Fe_3O_4$ with (220), (222), and (400) planes, respectively (JCPDS 01-071-6339). It is well known that the MgO of $Fe_3O_4$/MgO nanocomposite could be hydrated by water to produce $Mg(OH)_2$, which covers the surface. The produced $Mg(OH)_2$ can partially dissociate to release $OH^-$. Thus, Pb(II) easily assembles with $OH^-$ and forms $Pb(OH)_2$. Due to the lower stability of $Pb(OH)_2$(s), it can react with $CO_2$ dissolved in the solution to produce $Pb_3(CO_3)_2(OH)_2$ (Zhang *et al*., 2014) The presence of these $Fe_2O_3$ impurity peaks suggests the partial oxidation of $Fe_3O_4$ in aqueous solution. The observed changes in crystal structure and phase provide confirmation of the adsorption process.

**Fourier-transform infrared spectroscopy (FTIR)**

According to the FTIR analysis in Supplementary Figure S3 [curve (a)], results confirmed the presence of MgO and $Fe_3O_4$ in the $Fe_3O_4$/MgO adsorbent composition, and evidence of Pb(II) adsorbed $Fe_3O_4$/MgO nanocomposite (Pb(II)-$Fe_3O_4$/MgO) [curve (b)] was obtained in the range of 400 – 4000 $cm^{-1}$. The presence of the strong, sharp

band at 1738 $cm^{-1}$ in the $Fe_3O_4$/MgO nanocomposite suggests the involvement of organic compounds with C=O stretching vibrations. The specific origin of these compounds could vary depending on the synthesis method, reaction conditions, and post-synthesis treatments applied to the nanocomposite. Exposure to air or oxygen during synthesis or storage can lead to the oxidation of organic compounds present in the system, resulting in the formation of carbonyl groups. This surface oxidation process can occur on both the $Fe_3O_4$ nanoparticles and the MgO coating, leading to the presence of C=O stretching vibrations in the nanocomposite. The medium peak at approximately 1216 $cm^{-1}$ in the $Fe_3O_4$/MgO nanocomposite corresponds to C-N stretching vibrations. This may arise from the nitrogen atom present in the CTAB molecule, which contains a quaternary ammonium cation. Additionally, ammonia used in the synthesis process can provide nitrogen, facilitating the formation of C-N bonds with organic compounds present in the reaction mixture. The bands that appeared in the low wavenumber region are associated with characteristic peaks of metal-oxygen (M-O) bonds. The bands below 1000 $cm^{-1}$ are related to Mg-O absorption. This indicates the presence of MgO nanoparticles in calcined compounds. The frequency of heteropolar diatomic MgO stretching is confirmed by the peak at 874 $cm^{-1}$. The bands at 442 $cm^{-1}$ and 536.7 $cm^{-1}$ are referred to as $Fe_3O_4$, and those bands are associated with the magnetic property on the adsorbent surface. The observed bands in this analysis appear at higher wavenumbers compared to the standard, indicating a shift caused by the alteration of electron density distribution on the surface of nanoparticles. This change in electron density results from the interaction between the nanoparticles and the surrounding environment, leading to the strengthening of chemical bonds within the nanocomposite structure. The $Fe_3O_4$/MgO nanocomposite also shows similar absorption peaks. A medium sharp peak appeared at 1365 $cm^{-1}$, which is associated with the O-H bending vibration of hydroxyl groups. This vibration is attributed to the presence of residual hydroxyl groups from the hydroxide solution used during the synthesis process. This suggests the formation of a magnesium hydroxide ($Mg(OH)_2$) layer with magnetite. This peak is weaker than curve (b) due to antisymmetric stretching in $Mg(OH)_2$ crystal structure. In addition, this fact also serves as an indication that the calcination process at 400 ℃ for 2 hours has resulted in the transformation of the structure compound from the hexagonal $Mg(OH)_2$ form to the cubic MgO form. After the Pb(II) adsorption, MgO reverted to $Mg(OH)_2$ due to the water present in the Pb(II) solution and the bands observed for the dried sample. Multiple broad peaks at 2970 $cm^{-1}$ reveal the asymmetric vibration of the C-H ($-CH_2$) stretch arising from the alkyl chains of CTAB. Curve (b) shows the FTIR spectra of Pb(II)-$Fe_3O_4$/MgO obtained in the range of 400–4000 $cm^{-1}$. The new peaks that arose between 1092-874 $cm^{-1}$ indicate the presence of Pb–O. The weak band at 1092 $cm^{-1}$ corresponds to the stretching vibration of $CO_3^{2-}$ due to the formation of $Pb_3(CO_3)_2(OH)_2$ on the surface of $Fe_3O_4$/MgO nanocomposite. The change in IR intensity between 1100 $cm^{-1}$ and 870 $cm^{-1}$ suggested Pb(II) adsorption, which occurred in the form of Fe-O-Mg-O-Pb(II), with bending modes at 1092 $cm^{-1}$ and 874 $cm^{-1}$. New absorption peaks observed at 3692 $cm^{-1}$ correspond to O-H stretching vibration due to the PbO-adsorbed water moiety on the $Fe_3O_4$/MgO surface (Kawsihan *et al*., 2023). Pb(II) can combine with $OH^-$ ions to form the insoluble hydroxide $Pb(OH)_2$, which can further react with dissolved $CO_2$ to form $Pb_3(CO_3)_2(OH)_2$. The band at 2359 $cm^{-1}$ disappeared in curve (b), while it was present in curve (a), is ascribed to carbonate stretching and carbonate ions attached with Pb(II). After adsorption, bands at 1432 $cm^{-1}$ can be attributed to $CO_3^{2-}$ groups chemisorbed over the MgO surface. The peaks at 442 $cm^{-1}$ and 536.7 $cm^{-1}$ were shifted to 445 $cm^{-1}$ and 537.2 $cm^{-1}$ after Pb(II) adsorption, thereby, indicating that the MgO surface is covered by PbO and cation exchange between Mg(II) and Pb(II) may take place.

**Vibrating sample magnetometry (VSM)**

VSM analysis conducted on the $Fe_3O_4$/MgO nanocomposite revealed a magnetization saturation of 32.02 emu $g^{-1,}$ as shown in Supplementary Figure S4. This finding indicates that the nanocomposite exhibits superparamagnetic behaviour. The observed magnetization saturation is a crucial characteristic that highlights the potential of the $Fe_3O_4$/MgO nanocomposite for efficient magnetic separation and recovery in various wastewater treatment applications. The high saturation magnetization value signifies that the nanocomposites possess strong magnetic properties, enabling them to respond effectively to external magnetic fields. It allows for easy and rapid separation of the nanocomposite from the treated water using magnetic field-based separation techniques. This magnetic responsiveness facilitates the removal of the adsorbent from the water after the adsorption of Pb(II) ions, simplifying the purification process. Additionally, the high magnetization saturation value indicates that the $Fe_3O_4$/MgO nanocomposite can be easily regenerated and reused. Once separated from the water, the nanocomposite can be subjected to external magnetic fields to remove any remaining adsorbed Pb(II) ions. This capability of repeated use enhances the cost-effectiveness and sustainability of the nanocomposite as an adsorbent material. Moreover,

the magnetization saturation value provides valuable insights into the overall stability and dispersibility of the $Fe_3O_4$/MgO nanocomposite. It suggests that the magnetic $Fe_3O_4$ component within the nanocomposite contributes significantly to their stability, allowing them to maintain their magnetic properties during the adsorption process. These attributes make the nanocomposite a promising candidate for wastewater treatment applications, offering enhanced performance and reusability in the removal of Pb(II) ions from contaminated water sources.

**Effect of adsorbent dose**

Dosage optimization experiments were conducted using Pb(II) solutions prepared from $Pb(NO_3)_2$ salt. The adsorption efficiency of Pb(II) ions onto $Fe_3O_4$/MgO nanocomposite increased with increasing adsorbent dosage up to a certain point and then reached a plateau. Figure 1a shows the variation in adsorption efficiency with different adsorbent dosages. The maximum adsorption efficiency was observed at 0.25 g $L^{-1}$, where a significant reduction in Pb(II) concentration was achieved. The adsorption capacity of the $Fe_3O_4$/MgO nanocomposite also followed a similar trend as the adsorption efficiency. Initially, the total adsorption increased with increasing dosage due to the availability of more adsorption sites. However, the adsorption capacity per unit mass (mg $g^{-1}$) typically decreases with higher dosages because the additional adsorbent does not proportionally increase the amount of adsorbate. However, beyond 0.25 g $L^{-1}$, no significant changes in adsorption capacity were observed. The optimal adsorbent dosage of 0.25 g $L^{-1}$ can be attributed to the balance between the available adsorption sites on the $Fe_3O_4$/MgO nanocomposite and the concentration of Pb(II) ions in the solution. At lower dosages, the number of active sites may be insufficient to accommodate all the Pb(II) ions, leading to incomplete adsorption. On the other hand, at higher dosages, excess adsorbent might result in aggregation or agglomeration, limiting the accessibility of active sites. This optimum dosage ensures the availability of sufficient active sites on the adsorbent while avoiding excessive aggregation.

**Effect of initial concentration**

The initial concentration of Pb(II) ions varied within the range of 400 to 1000 mg $L^{-1}$ while keeping other parameters constant. Figure 1b presents the variation in adsorption efficiency with different initial concentrations. The maximum removal efficiency was observed at an initial concentration of 600 mg $L^{-1}$, resulting in a significant reduction in Pb(II) concentration. The adsorption capacity of the $Fe_3O_4$/MgO nanocomposites for Pb(II) ions also followed a similar trend as the adsorption efficiency. The adsorption capacity increased with the initial concentration up to 600 mg $L^{-1}$ and then reached a plateau, suggesting saturation of the adsorption sites. The optimum initial concentration of 600 mg $L^{-1}$ can be attributed to a balance between the availability of Pb(II) ions and the adsorption capacity of the $Fe_3O_4$/MgO nanocomposite. At lower initial concentrations, the limited number of metal ions may result in underutilization of the adsorbent's capacity. Conversely, at higher initial concentrations, the active sites on the adsorbent may become overwhelmed, leading to reduced adsorption efficiency.

**Effect of pH**

The initial concentration of Pb(II) ions was kept constant, while the pH of the solution was adjusted within the range of 4 to 10 using HCl and NaOH. The removal efficiency of Pb(II) ions using $Fe_3O_4$/MgO nanocomposite was strongly influenced by the pH of the solution. Figure 1c illustrates the variation in adsorption efficiency with different pH values. The maximum removal efficiency was observed at pH 7, resulting in a significant reduction in Pb(II) concentration. The surface charge of both Pb(II) ions and the $Fe_3O_4$/MgO nanocomposite is crucial in adsorption. At low pH values (pH < 7), the surface of the adsorbent is positively charged due to the protonation of surface hydroxyl groups. However, since Pb(II) ions are also positively charged, the adsorption in acidic conditions is less favourable due to electrostatic repulsion. As the pH increases and approaches neutral conditions, the adsorbent surface becomes less positively charged, reducing the repulsion between the adsorbent and Pb(II) ions, which enhances adsorption. At high pH values (pH > 7), the surface of the adsorbent becomes negatively charged due to the deprotonation of surface hydroxyl groups. This negatively charged surface can interact favourably with the positively charged Pb(II) ions through electrostatic attraction. However, at very high pH values, the formation of $Pb(OH)_2$ precipitates can occur, which reduces the amount of Pb(II) ions available for adsorption. Therefore, the optimized pH of 7 can be attributed to a balance between surface charge interactions and the prevention of $Pb(OH)_2$ precipitation. The optimized pH of 7 can be attributed to the surface charge interaction between the Pb(II) ions and the adsorbent.

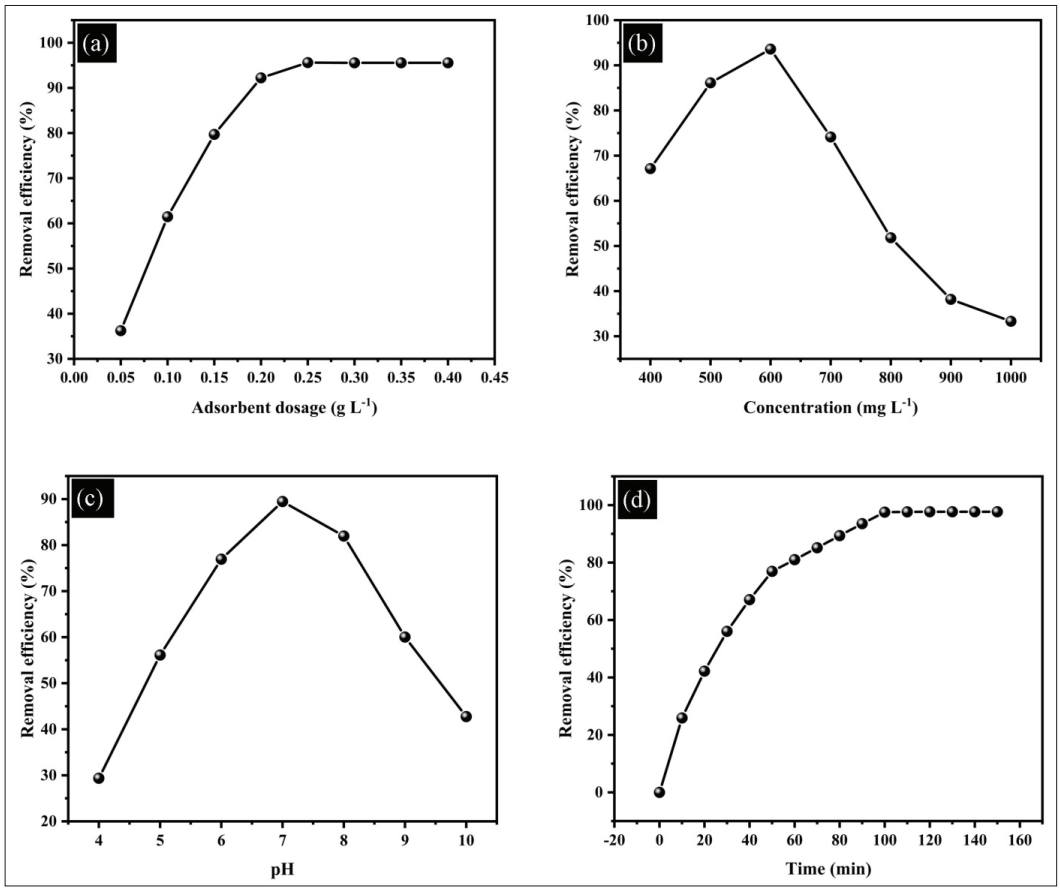


**Figure 1:** (a) The effect of the rate of adsorbent dose (b) The effect of initial concentration of lead (c) Effect of pH on the efficiency of removing lead (d) Effect of contact time on the efficiency of removing lead

At pH 7, the adsorbent surface is slightly negatively charged, which promotes the electrostatic attraction and adsorption of Pb(II) ions. Additionally, at this pH, the hydroxylation of Pb(II) ions is insignificant, preventing the formation of $Pb(OH)_2$ precipitates, which could reduce the adsorption efficiency. Therefore, pH 7 provides the optimum conditions for maximizing the electrostatic attraction between the adsorbent surface and Pb(II) ions. This study demonstrated that the maximum removal efficiency was achieved at pH 7, which can be attributed to the surface charge interaction between Pb(II) ions and the adsorbent. The slightly negatively charged surface of the adsorbent at pH 7 facilitated the electrostatic attraction and enhanced the adsorption of Pb(II) ions. Additionally, chemical binding or complexation, with a significant covalent component, may also play a crucial role in the adsorption process.

## Effect of reaction time

The initial concentration of Pb(II) ions was kept constant, and the contact time varied from 0 to 150 minutes. Figure 1d illustrates the variation in adsorption efficiency with different contact times. The adsorption efficiency increased rapidly within the first 50 minutes, followed by a slower increase until reaching equilibrium at 100 minutes. After 120 minutes, there was no significant change in efficiency, indicating the attainment of equilibrium. The initial rapid increase in adsorption efficiency within the first 50 minutes can be attributed to the availability of a large number of active sites on the adsorbent surface. During this stage, the concentration gradient between the solution and the adsorbent surface is high, leading to rapid diffusion of Pb(II) ions to the adsorbent surface and subsequent adsorption. The

adsorption process involves surface complexation, where Pb(II) ions form coordination bonds with active sites on the adsorbent surface. After the initial rapid increase, the adsorption efficiency gradually increases at a slower rate. This can be attributed to the reduction in the concentration gradient between the solution and the adsorbent surface as more Pb(II) ions are adsorbed. As the adsorption sites become occupied, the diffusion of Pb(II) ions to the remaining available sites becomes slower, resulting in a slower increase in adsorption efficiency. At 100 minutes, the adsorption efficiency starts to reach its maximum, indicating that the adsorption sites are nearly saturated. This study demonstrated that equilibrium was reached at 120 minutes, with an initial rapid increase in efficiency within the first 50 minutes. The adsorption kinetics and equilibrium dynamics suggest that the adsorption process involves surface complexation and diffusion of Pb(II) ions to the active sites on the adsorbent surface.

### *Kinetics and isotherms of Pb (II) adsorption*

Equilibrium studies were conducted to investigate the adsorption behaviour of Pb(II) ions on $Fe_3O_4$/MgO nanocomposite (Figure 2a and 2b). The experiment was performed under optimized conditions, including a pH of 7, adsorbent dosage of 0.25 g $L^{-1}$, initial Pb(II) concentration of 600 mg $L^{-1}$, and reaction time of 120 minutes. The equilibrium was achieved at 100 minutes, and further analysis was carried out at 120 minutes to ensure that equilibrium was reached. During the adsorption process, the concentration of Pb(II) ions gradually decreased with time. In the initial 50 minutes, a rapid reduction in concentration was observed, indicating a high adsorption rate. Subsequently, from 50 to 100 minutes, the concentration reduction slowed down, and the equilibrium state was reached. This behaviour suggests that the adsorption process involved both a rapid surface adsorption phase and a slower intra-particle diffusion phase. The experimental adsorption capacity and removal efficiency of $Fe_3O_4$/MgO nanocomposite for Pb(II) ions were determined to be approximately 2399 mg $g^{-1}$ and 99.98%, respectively. This high adsorption capacity indicates the strong affinity of $Fe_3O_4$/MgO nanocomposite towards Pb(II) ions and highlights their potential as efficient adsorbents for the removal of heavy metal pollutants from aqueous solutions. Comparison with previous literature findings related to the removal of Pb(II) ions using MgO nanoparticles revealed that the adsorption capacity of $Fe_3O_4$/MgO nanocomposite in this study is significantly higher (Supplementary Table S2).

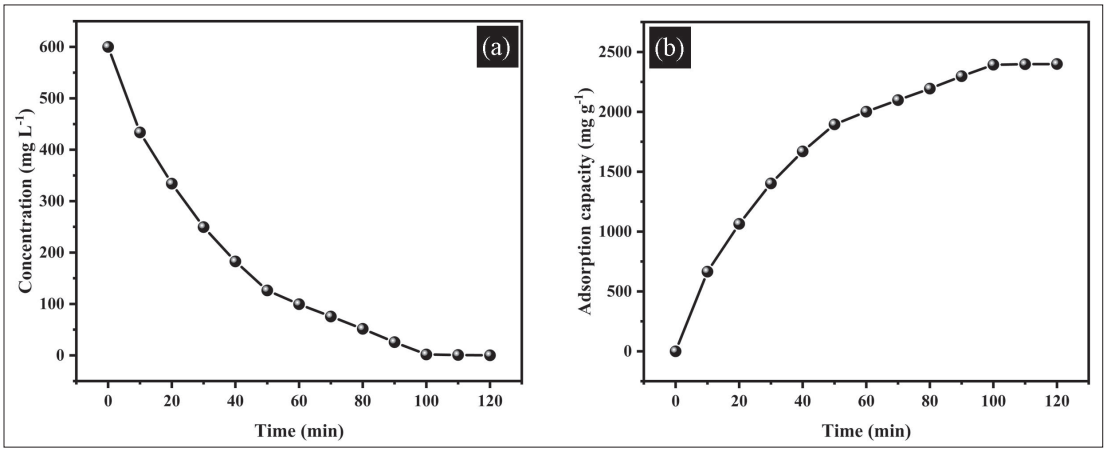


**Figure 2:** (a) Concentration variation with time (b) Adsorption capacity variation with time for Pb(II) adsorption

This enhancement can be attributed to the unique properties of the $Fe_3O_4$/MgO nanocomposite, such as their high surface area, well-defined morphology, and synergistic effects between $Fe_3O_4$ and MgO nanoparticles. The obtained equilibrium at 120 minutes, the gradual decrease in concentration with time, and the high experimental adsorption capacity of 2399.44 mg $g^{-1}$ highlight the effectiveness of the $Fe_3O_4$/MgO nanocomposite as adsorbents. The results consistently highlight the high adsorption capacity and efficiency of MgO nanoparticles in removing Pb(II) from aqueous solutions. The findings from these studies support and complement the superior adsorption performance of $Fe_3O_4$/MgO nanocomposites observed.

Adsorption kinetics of Pb(II) ions on $Fe_3O_4$/MgO nanocomposite was investigated using the pseudo-first-order, pseudo-second-order, Webber Morris model, and liquid film diffusion model (Figures 3a to 3d; Table 1). The pseudo-first-order model assumes that the adsorption rate is proportional to the difference between the equilibrium and adsorbate concentrations. The pseudo-second-order model considers the adsorption process as chemisorption involving the sharing or exchange of electrons between the adsorbate and adsorbent. The kinetic rate constants and correlation coefficients ($R^2$) were determined for both models. For the pseudo-first-order model, the calculated rate constant ($k_1$) was found to be $5.52\times10^{-2}$ $min^{-1}$, and the correlation coefficient ($R^2$) was 0.81. However, the experimental data did not fit well with the pseudo-first-order model, as indicated by the lower correlation coefficient.

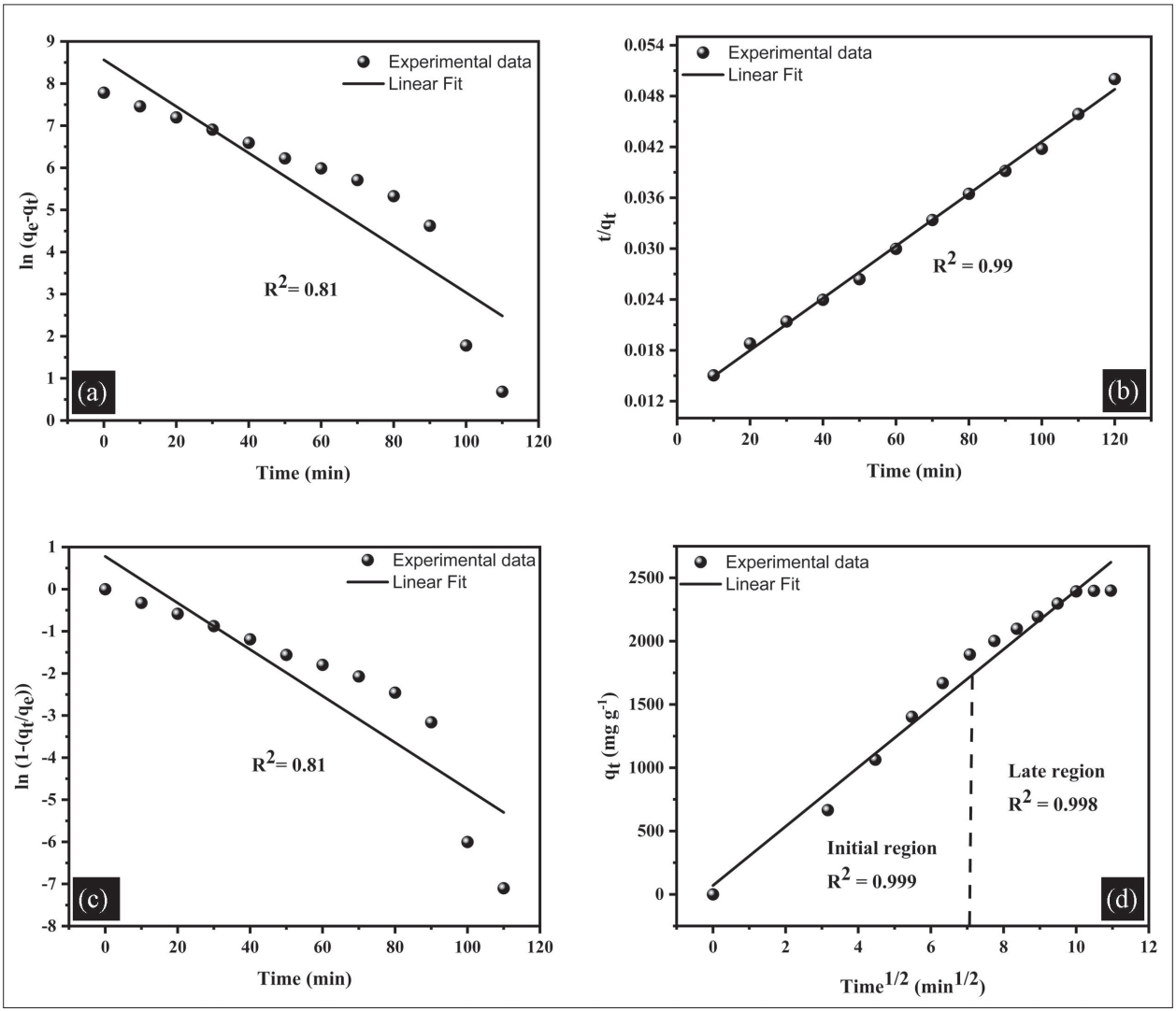


**Figure 3:** (a and b) Nonlinear pseudo-first-order and pseudo-second-order kinetic plots; (c and d) the liquid film diffusion model and intra-particle diffusion model plot of Pb(II) on $Fe_3O_4$/MgO nanocomposite

**Table 1:** Fitting parameters of pseudo first order, pseudo second order, liquid film diffusion model, and IPD (Intra-particle diffusion) rate constants and intercept values of Webber and Morris for Pb(II) adsorption

| Kinetics model | Kinetic equation | Parameter | Value |
|---|---|---|---|
| Pseudo-first-order | $\ln(q_e - q_t) = \ln q_e - k_1 t$ | $q_e$ (mg $g^{-1}$) | 5223.43 |
| | | $k_1$ (× $10^{-2}$ $min^{-1}$) | 5.52 |
| | | $R^2$ | 0.81 |
| Pseudo-second-order | $\frac{t}{q_t} = \frac{1}{k_2 q_e^2} + \frac{1}{q_e} t$ | $q_e$ (mg $g^{-1}$) | 3247.04 |
| | | $k_2$ (×$10^{-6}$ g $mg^{-1}$ $min^{-1}$) | 7.19 |
| | | $R^2$ | 0.997 |
| Liquid film diffusion | $\ln(1 - (\frac{q_t}{q_e})) = -k_{LF} \times t$ | $k_{LF}$ (× $10^{-2}$ $min^{-1}$) | 5.52 |
| | | $R^2$ | 0.81 |
| Intra-particle diffusion | $q_t = k_{diff} t^{1/2} + C$ | Initial region | |
| | | $k_{dif}$ (mg $g^{-1}$ $min^{-0.5}$) | 316.98 |
| | | C | -341.47 |
| | | $R^2$ | 0.999 |
| | | Late region | |
| | | $k_{dif}$ (mg $g^{-1}$ $min^{-0.5}$) | 174.45 |
| | | C | 642.72 |
| | | $R^2$ | 0.998 |

On the other hand, the pseudo-second-order model showed a better fit to the experimental data. The calculated rate constant ($k_2$) was $7.19\times10^{-6}$ g $mg^{-1}$ $min^{-1}$, and the correlation coefficient ($R^2$) was 0.997. The higher correlation coefficient suggests that the pseudo-second-order model more accurately describes the adsorption kinetics of Pb(II) ions on $Fe_3O_4$/MgO nanocomposite. Furthermore, the Webber Morris model was applied to evaluate the adsorption mechanism. The model consists of two regions: an initial region where the adsorption process is dominated by external film diffusion and a late region where intra-particle diffusion becomes the rate-controlling step. The initial region exhibited better efficiency ($R^2$ = 0.999) with a higher adsorption rate constant ($k_{diff}$ = 316.98 mg $g^{-1}$ $min^{-0.5}$) compared to the late region ($k_{diff}$ = 174.45 mg $g^{-1}$ $min^{-0.5}$). This indicates that external film diffusion played a significant role in the early stages of the adsorption process. Additionally, the liquid film diffusion model was considered to understand the mass transfer mechanisms during adsorption. The model accounts for the resistance of mass transfer in the liquid film surrounding the adsorbent particles. The calculated film diffusion coefficient $k_{LF}$ was found to be $5.524\times10^{-2}$ $min^{-1}$. This value indicates the effectiveness of the liquid film diffusion process in the overall adsorption mechanism. Comparing the results of the different kinetic models, it can be concluded that the pseudo-second-order model provided the best fit to the experimental data, suggesting that the adsorption of Pb(II) ions on $Fe_3O_4$/MgO nanocomposite follows chemisorption kinetics. The Webber-Morris model indicated the importance of external film diffusion in the initial stages of adsorption. Furthermore, the liquid film diffusion model highlighted the role of mass transfer through the liquid film surrounding the adsorbent particles. These findings contribute to a better understanding of the adsorption kinetics and mechanisms involved in the removal of Pb(II) ions using $Fe_3O_4$/MgO nanocomposite.

The results of the isotherm models, namely Langmuir, Freundlich, and Temkin, are presented and discussed in this section (Figure 4a, 4b and 4c; Table 2). These models were used to analyze the adsorption behaviour of Pb(II) ions on $Fe_3O_4$/MgO nanocomposite. The Langmuir isotherm model assumes monolayer adsorption on a homogeneous surface with a limited number of adsorption sites. The Freundlich isotherm model describes the adsorption on heterogeneous surfaces with multilayer adsorption. The Temkin isotherm model assumes a uniform distribution of binding energies and accounts for the effects of adsorbate-adsorbent interactions. In our study, the experimental data were fitted to these isotherm models using regression analysis. The regression coefficients ($R^2$) were used to evaluate the goodness of fit for each model.

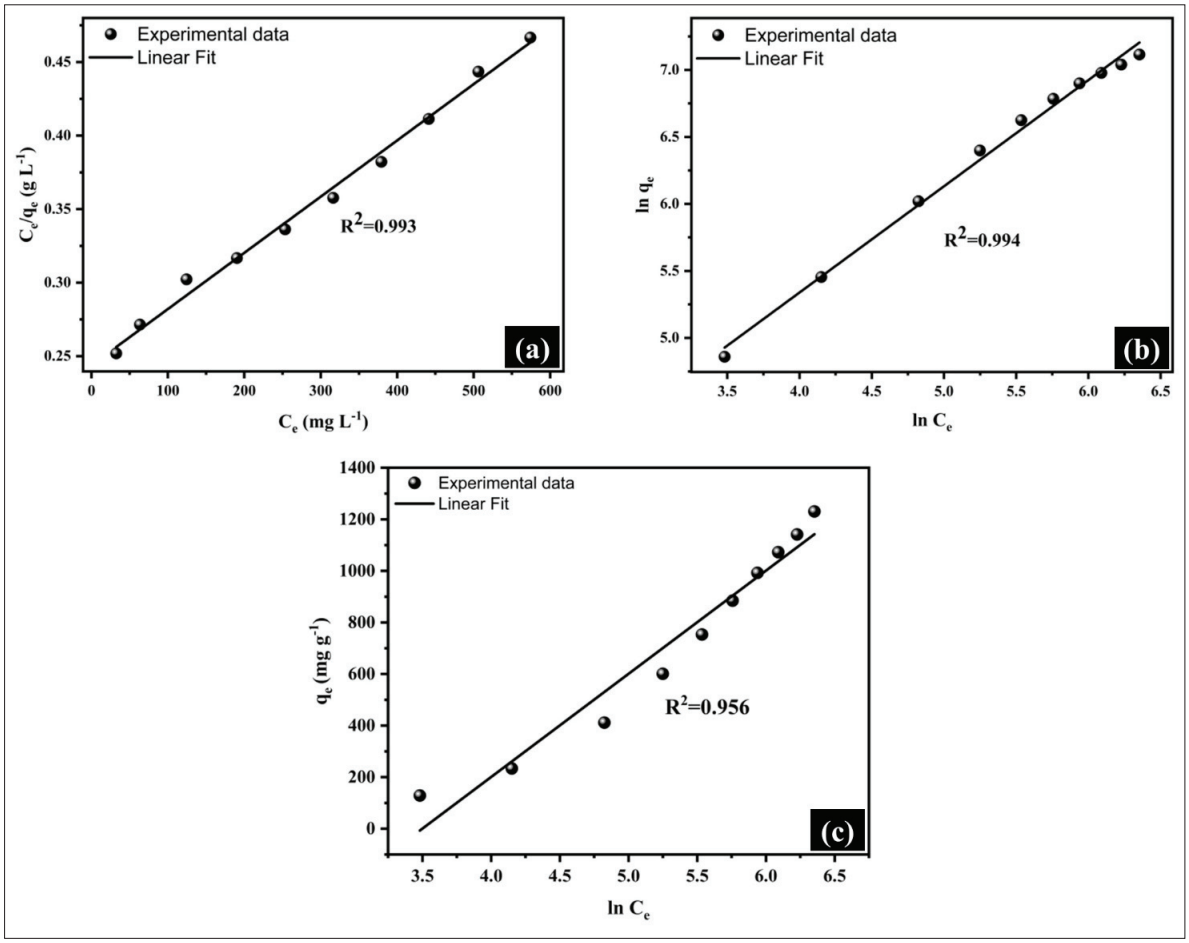


**Figure 4:** (a.) Langmuir model fit and (b.) Freundlich model fit (c.) Temkin model for adsorption of Pb(II) on $Fe_3O_4$/MgO nanocomposite

**Table 2:** Fitting parameters of Langmuir model, Freundlich model, and Temkin model for Pb(II) adsorption

| Isotherm model | Equation | Parameter | Value |
|---|---|---|---|
| Langmuir | $\frac{C_e}{q_e} = \frac{1}{q_m k_L} + \frac{C_e}{q_m}$ | $q_m$ (mg $g^{-1}$) | 2615.35 |
| | | $K_L$ (× $10^{-3}$ L $mg^{-1}$) | 1.57 |
| | | $R^2$ | 0.993 |
| Freundlich | $\ln q_e = \ln k_F + \frac{1}{n} \ln C_e$ | n | 1.26 |
| | | $K_F$ (L $mg^{-1}$) | 8.75 |
| | | $R^2$ | 0.994 |
| Temkin | $q_e = \frac{RT}{b} \ln k_T + \frac{RT}{b} \ln C_e$ | b (J $mol^{-1}$) | 6.2 |
| | | $K_T$ (L $mg^{-1}$) | $3.03 \times 10^{-2}$ |
| | | $R^2$ | 0.956 |

The results showed that the Freundlich model provided a slightly better regression coefficient ($R^2$ = 0.994) compared to the Langmuir model ($R^2$ = 0.993), while both models performed significantly better than the Temkin model ($R^2$ = 0.956) for the removal of Pb(II) ions using $Fe_3O_4$/MgO nanocomposite. This indicates the adsorption process follows a multilayer adsorption mechanism on a heterogeneous surface. The Langmuir and Temkin models, although not providing as good a fit as the Freundlich model, still showed reasonable correlation coefficients. This suggests that there may be some monolayer adsorption and interactions between the adsorbate and adsorbent surface. Therefore, specific values of the Freundlich constant ($k_F$) and exponent (n) should be discussed. For instance, a high value of the constant ($k_F$ = 8.75) implies a higher adsorption capacity, while an exponent (n) close to unity (n = 1.26) suggests favourable adsorption intensity (Table 2). The higher adsorption capacity ($k_F$) and favourable adsorption intensity (n) indicate the effectiveness of the nanocomposite in removing Pb(II) ions from aqueous solutions. Overall, the results from the isotherm models, along with the specific parameter values (Table 2), confirm that the Freundlich model provides a better fit to the experimental data and highlights the significance of adsorption intensity in the removal of Pb(II) ions using $Fe_3O_4$/MgO nanocomposite. By fitting the experimental data to the Temkin isotherm equation, we can obtain the values of the Temkin constant (b = 6.2) and the equilibrium binding constant ($K_{Temkin}$ = $3.03\times10^{-2}$), which provide insights into the adsorption process. The obtained results showed that the Temkin model provided a relatively lower regression coefficient (0.956) compared to the Freundlich model. This suggests that the Temkin model may not be the most suitable model for describing the adsorption behaviour of Pb(II) ions on $Fe_3O_4$/MgO nanocomposite in our experimental conditions. However, it is important to note that the applicability of the Temkin model depends on various factors such as the nature of the adsorbate and adsorbent, as well as the experimental conditions. Therefore, further investigations and variations in experimental parameters may be required to better understand the suitability and limitations of the Temkin model for the adsorption of Pb(II) ions using $Fe_3O_4$/MgO nanocomposite.

In conclusion, while the Temkin model was utilized in our study, the obtained results indicated that the Freundlich model provided a better fit to the experimental data. This suggests that the Freundlich model may be more appropriate for describing the adsorption behaviour of Pb(II) ions on $Fe_3O_4$/MgO nanocomposite. However, further research and analysis are needed to gain a comprehensive understanding of the adsorption mechanism and optimize the adsorption process for effective removal of Pb(II) ions. Overall, the results of the isotherm models indicate that the adsorption of Pb(II) ions on $Fe_3O_4$/MgO nanocomposite is influenced by both monolayer and multilayer adsorption mechanisms.

## CONCLUSION

The removal of Pb(II) ions using $Fe_3O_4$/MgO nanocomposite has been successfully investigated, and the following conclusions can be drawn from the experimental results. Firstly, the initial concentration of Pb(II) ions significantly influenced the adsorption capacity of the nanocomposite. Higher initial concentrations resulted in higher adsorption capacities, indicating that the adsorption process is concentration-dependent. Secondly, the adsorbent dosage played a crucial role in the adsorption efficiency. Increasing the dosage of $Fe_3O_4$/MgO nanocomposite led to an increase in the adsorption efficiency, reaching a maximum point where further increase in dosage did not significantly affect the adsorption efficiency. Thirdly, the pH of the solution had a notable impact on the adsorption process. The highest adsorption capacity was observed at an optimal pH value, suggesting the pH-dependent nature of the adsorption mechanism. The nanocomposite exhibited better adsorption performance at neutral pH (pH = 7). Furthermore, the reaction time was found to be an essential parameter in achieving equilibrium adsorption. The adsorption process reached equilibrium within a specific time period, and prolonged contact time did not significantly affect the adsorption capacity. The experimental adsorbent capacity and removal efficiency were determined as 2399.44 mg $g^{-1}$ and 99.98%, respectively. The Freundlich model provided a better fit, indicating multilayer adsorption on a heterogeneous surface. The pseudo-second-order model described the kinetics, suggesting chemisorption as the rate-controlling step. SEM-EDS, XRD, FTIR, and VSM techniques confirmed successful nanocomposite synthesis, revealing pyramid-like and irregular crystal morphology, crystalline cubic $Fe_3O_4$ and MgO phases, chemical interactions, and superparamagnetic behaviour. These findings contribute to understanding Pb(II) ion adsorption using $Fe_3O_4$/MgO nanocomposite, highlighting their promising applications in environmental remediation. This study proved the enhancement of the removal efficiency and adsorption capacity for Pb(II) ions using sol-gel synthesized $Fe_3O_4$/MgO nanocomposite, compared with previously reported literature.

**Funding**

This research was funded by the Science batch of 1976-1980 of the Faculty of Science, University of Peradeniya, Sri Lanka,

**Acknowledgment**

This paper is dedicated to the memory of our co-author, Dr. Buddhika S. Dassanayake, who tragically passed away on December 25, 2023. Despite his untimely demise, Dr. Dassanayake's dedication and expertise left an indelible mark on the development of this work. His visionary leadership played a pivotal role in shaping the trajectory of this project. The collaborative spirit and collective effort that has shaped this manuscript are forever indebted to Dr. Dassanayake's significant role. His impact on this project, his academic legacy, and his enduring influence within the scientific community will be cherished and remembered with deep gratitude.

## REFERENCES

Cabeza, A., & Aranda, M.A.G. (1996). Ab initio powder structure determination and thermal behavior of a new lead (II) phenylphosphonate, Pb ($O_3PC_6H_5$). *Acta Crystallographica Section B: Structural Science, Crystal Engineering and Materials, 52*, 982-988. https://doi.org/10.1107/S0108768196006829

Habiby, S.R., Esmaeili, H., & Foroutan, R. (2019). Magnetically modified MgO nanoparticles as an efficient adsorbent for phosphate ions removal from wastewater. *Separation Science and Technology, 55*(11), 1-12. https://doi.org/10.1080/01496395.2019.1617744

Lidsky, T.I., & Schneider, J.S. (2003). Lead neurotoxicity in children: Basic mechanisms and clinical correlates. *Brain, 126*(1), 5-19. https://doi.org/10.1093/brain/awg014

Minju, N., Swaroop, K.V., Haribabu, K., Sivasubramanian, V., & Senthil, P. (2015). Removal of fluoride from aqueous media by magnesium oxide-coated nanoparticles. *Desalination and Water Treatment, 53*(11), 2911-2920. https://doi.org/10.1080/19443994.2013.868837

Nagarajah, R., Wong, K. T., Lee, G., Chu, K. H., Yoon, Y., Kim, N. C., & Jang, M. (2017). Synthesis of a unique nanostructured magnesium oxide coated magnetite cluster composite and its application for the removal of selected heavy metals. *Separation and Purification Technology, 174*, 290-300. https://doi.org/10.1016/j.seppur.2016.11.008

Namvar-Mahboub, M., Khodeir, E., Bahadori, M., & Mahdizadeh, S.M. (2020). Preparation of magnetic MgO/$Fe_3O_4$ via the green method for competitive removal of Pb and Cd from aqueous solution. *Colloids and Surfaces, 589,* Article 124419. https://doi.org/10.1016/j.colsurfa.2020.124419

Salem, A. M., & Ahmed, M. A. (2016). Selective adsorption of amaranth dye on $Fe_3O_4$/MgO nanoparticles. *Journal of Molecular Liquids, 219*, 780-788. https://doi.org/10.1016/j.molliq.2016.03.084

Zhang, L., Zhu, W., Zhang, H., Bi, S., & Zhang, Q. (2014). Hydrothermal-thermal conversion synthesis of hierarchical porous MgO microrods as efficient adsorbents for lead (II) and chromium (VI) removal. *RSC Advances, 4*(58), 30542-30550. https://doi.org/10.1039/C4RA03971H

Kawsihan, A., Dissanayake, D. M. S. N., Rathuwadu, N. P. W., Perera, H. C. S., Dayananda, K. E. D. Y. T., Koswattage, K. R., Mahadeva, R., Ganguly, A., Das, G., & Mantilaka, M. M. M. G. P. G. (2023). Synthesis of an eco-inspired anticorrosive composite for mild steel applications. *RSC Advances*, *13*(41), 28852-28860. https://doi.org/10.1039/D3RA02857G

Perera, H. C. S., Gurunanthanan, V., Singh, A., Mantilaka, M. M. M. G. P. G., Das, G., & Arya, S. (2024). Magnesium oxide (MgO) nanoadsorbents in wastewater treatment: A comprehensive review. *Journal of Magnesium and Alloys*, *12*(5), 1709-1773. https://doi.org/10.1016/j.jma.2024.05.003

Sameera, S. A. L., Edirisinghe, N. P., Kannangara, Y. Y., Karunarathne, S., Koswattage, K. R., Perera, H. C. S., Das, G., Mantilaka, M. M. M. G. P. G., & Wijesinghe, W. P. S. L. (2023). Enhanced Wide Spectrum Photocatalytic Activity by in-Situ Magnetite-Graphite Nanoplatelets Heterostructure. *IEEE Access*, *11*(June), 68912-68924. https://doi.org/10.1109/ACCESS.2023.3290029

## Supplementary data

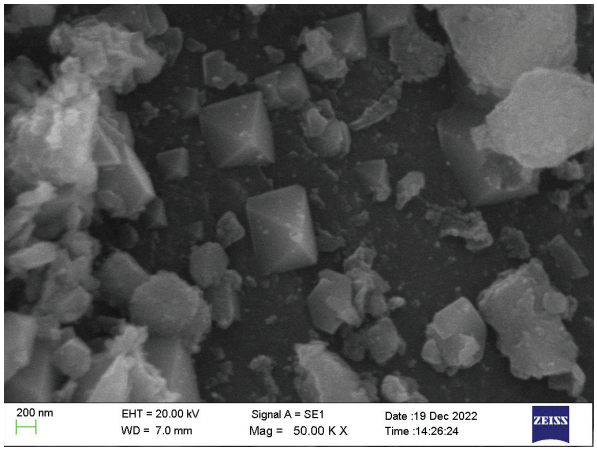


**Figure S1(a):** SEM image of $Fe_3O_4$/MgO nanocomposites

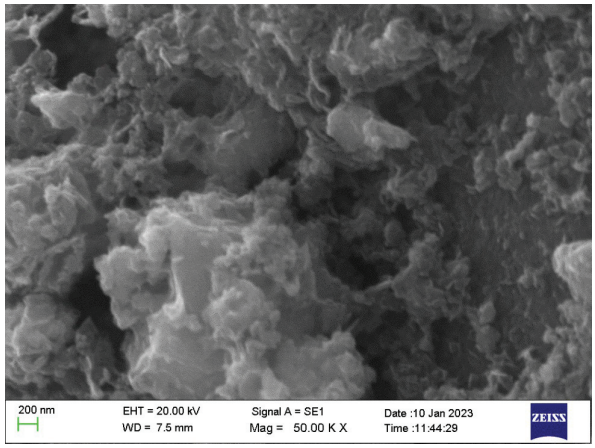


**Figure S1(b):** SEM image of Pb(II) adsorbed $Fe_3O_4$/MgO nanocomposites

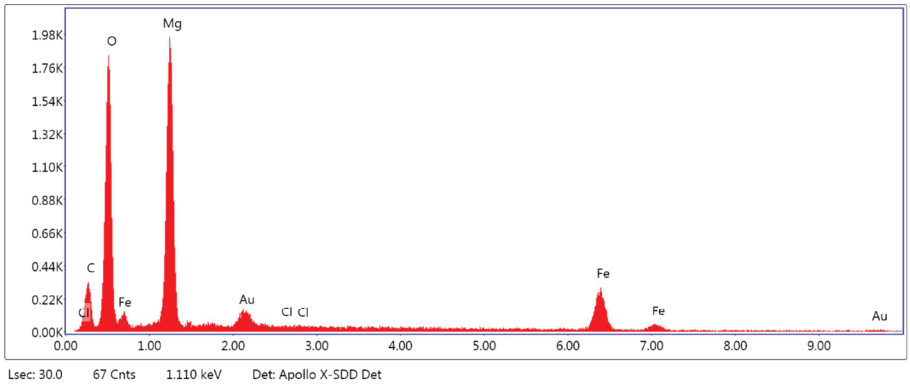


**Figure S1(c):** EDS analysis of $Fe_3O_4$/MgO nanocomposites

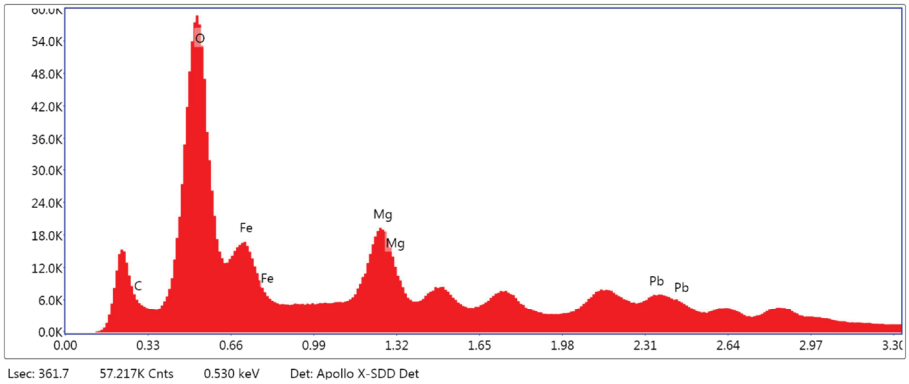


**Figure S1(d):** EDS analysis of $Fe_3O_4$/MgO nanocomposites

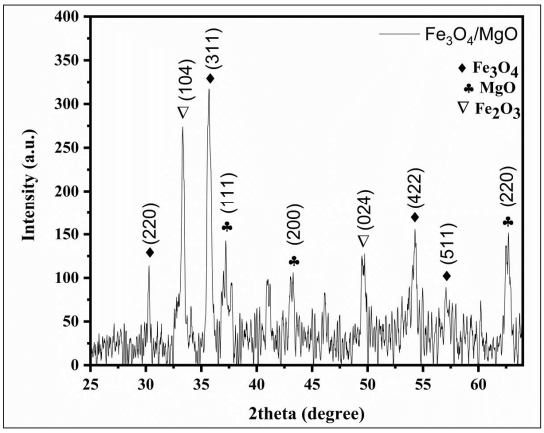


**Figure S2(a):** XRD analysis of $Fe_3O_4$/MgO nanocomposites

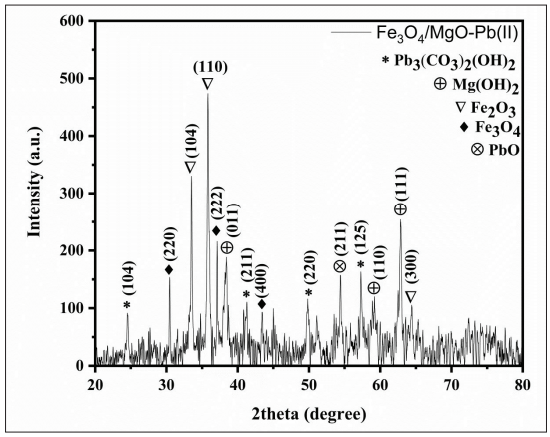


**Figure S2(b):** XRD analysis of Pb(II) adsorbed $Fe_3O_4$/MgO nanocomposites

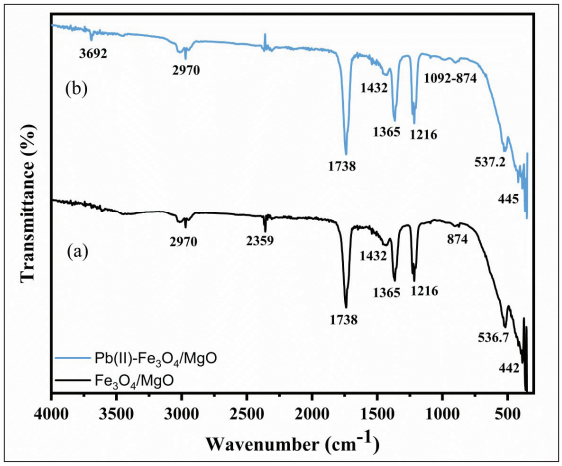


**Figure S3:** FTIR comparison between $Fe_3O_4$/MgO (Curve a) and Pb(II)-$Fe_3O_4$/MgO (Curve b)

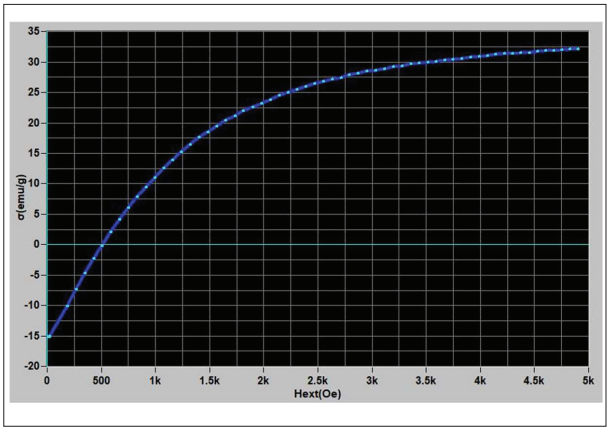


**Figure S4:** VSM data of $Fe_3O_4$/MgO nanocomposites (Hmax: 390 kA/m/4.896 kOe, Temperature: 272.3 K)

**Table S1:** Weight %, and Atomic % of $Fe_3O_4$/MgO nanocomposites, and Pb(II) adsorbed $Fe_3O_4$/MgO nanocomposites

| | $Fe_3O_4$/MgO nanocomposites | | Pb(II)-$Fe_3O_4$/MgO nanocomposites | |
|---|---|---|---|---|
| Elements | Weight% | Atomic% | Weight% | Atomic% |
| C K | 12.23 | 22.72 | 10.53 | 22.30 |
| O K | 30.00 | 41.85 | 37.61 | 59.79 |
| Fe L | 28.97 | 11.58 | 7.06 | 3.22 |
| MgK | 25.55 | 23.46 | 9.95 | 10.41 |
| PbM | | | 34.84 | 4.28 |

**Table S2:** Comparison of loading capacities of MgO with $Fe_3O_4$ for various adsorbate

| Adsorbent | Pollutant | Adsorption capacity (mg $g^{-1}$) | Reference |
|---|---|---|---|
| MgO/$Fe_3O_4$ | Phosphate | 2.95 | (Habiby *et al*., 2019) |
| $Fe_3O_4$/MgO | Amaranth dye | 37.98 | (Salem & Ahmed, 2016) |
| MgO cores with silica coated nano magnetite | Pb(II)<br>Cd(II)<br>Cu(II) | 238<br>85.1<br>33.5 | (Namvar-mahboub *et al*., 2020) |
| MgO-Coated $Fe_3O_4$ | F | 10.96 | (Minju *et al*., 2015) |
| $Fe_3O_4$/MgO | Pb(II) | 2399.44 (experimental) | This study |